Journal of Magnetic Resonance 257 (2015) 8–14

Contents lists available at ScienceDirect

Journal of Magnetic Resonance

journal homepage: www.elsevier.com/locate/jmr

Effect of magnetic field fluctuation on ultra-low field MRI measurements in the unshielded laboratory environment

Chao Liu [a,c], Baolin Chang [a,c], Longqing Qiu [a,c], Hui Dong [a,c,*], Yang Qiu [a,c], Yi Zhang [b,c], Hans-Joachim Krause [b,c], Andreas Offenhäusser [b,c], Xiaoming Xie [a,c]

[a] State Key Laboratory of Functional Materials for Informatics, Shanghai Institute of Microsystem and Information Technology (SIMIT), Chinese Academy of Sciences (CAS), Shanghai 200050, China

[b] Peter Grünberg Institute (PGI-8), Forschungszentrum Jülich (FZJ), D-52425 Jülich, Germany

[c] Joint Research Laboratory on Superconductivity and Bioelectronics, Collaboration between CAS–Shanghai, Shanghai 200050, China and FZJ, D-52425 Jülich, Germany

ARTICLE INFO

Article history:
Received 27 December 2014
Revised 6 April 2015
Available online 14 May 2015

Keywords:
dc SQUID
Ultra-low field MRI
Magnetic field fluctuation

ABSTRACT

Magnetic field fluctuations in our unshielded urban laboratory can reach hundreds of nT in the noisy daytime and is only a few nT in the quiet midnight. The field fluctuation causes the Larmor frequency f_L to drift randomly for several Hz during the unshielded ultra-low field (ULF) nuclear magnetic resonance (NMR) and magnetic resonance imaging (MRI) measurements, thus seriously spoiling the averaging effect and causing imaging artifacts. By using an active compensation (AC) technique based on the spatial correlation of the low-frequency magnetic field fluctuation, the field fluctuation can be suppressed to tens of nT, which is a moderate situation between the noisy daytime and the quiet midnight. In this paper, the effect of the field fluctuation on ULF MRI measurements was investigated. The 1D and 2D MRI signals of a water phantom were measured using a second-order low-T_c superconducting quantum interference device (SQUID) in three fluctuation cases: severe fluctuation (noisy daytime), moderate fluctuation (daytime with AC) and minute fluctuation (quiet midnight) when different gradient fields were applied. When the active compensation is applied or when the frequency encoding gradient field G_x reaches a sufficiently strong value in our measurements, the image artifacts become invisible in all three fluctuation cases. Therefore it is feasible to perform ULF-MRI measurements in unshielded urban environment without imaging artifacts originating from magnetic fluctuations by using the active compensation technique and/or strong gradient fields.

1. Introduction

In recent years there has been an increasing interest in ultra-low field (ULF) magnetic resonance imaging (MRI) using superconducting quantum interference devices (SQUIDs) for detection [1,2]. Compared to conventional MRI, ULF-MRI has a number of advantages, such as imaging in the presence of metallic objects [3] and enhanced T_1 contrast [4], and enables potential applications in anatomical and functional brain imaging [5–8].

One of the major challenges in ULF-MRI is the reduced sample magnetization, which is partially overcome by using a pre-polarization technique [9] and introducing a sensitive sensor such as a SQUID. Ambient environmental electromagnetic field noise deteriorates image quality, and the magnetic field interference including spatial inhomogeneity and temporal fluctuations can result in image distortions. As a result, ULF-MRI measurements are usually performed in a magnetically shielded room (MSR) [2,5–7], or in the Earth's magnetic field at remote outdoor locations far from any disruption to the local field homogeneity and from sources of ultra-low frequency noise [10].

However, the costly MSR or inconvenient outdoor operation blocks ULF-MRI from being an applicable technique. To develop a portable and inexpensive system without strict demands on the operating environment becomes a priority [11]. An ULF-MRI system was set up in the urban laboratory without any shielding. Because the environmental gradient field in our lab was relatively stable for hours, a static magnetic gradient tensor detection and compensation system was designed to effectively balance the environmental gradient field ranging between 1 and 5 μT/m [12]. An active compensation (AC) system based on spatial correlation of

* Corresponding author at: State Key Laboratory of Functional Materials for Informatics, Shanghai Institute of Microsystem and Information Technology (SIMIT), Chinese Academy of Sciences (CAS), Shanghai 200050, China. Fax: +86 21 62127493.

E-mail address: donghui@mail.sim.ac.cn (H. Dong).

http://dx.doi.org/10.1016/j.jmr.2015.04.014
1090-7807/

the low-frequency magnetic field fluctuation was developed to stabilize the temporal field fluctuations which may be as strong as 1 μT. With this compensation, ULF nuclear magnetic resonance (NMR) measurements were demonstrated [13].

In this paper, the effect of the magnetic field fluctuation on ULF-MRI measurements in the unshielded urban laboratory is investigated in detail. One-dimensional (1D) and two-dimensional (2D) ULF-MRI measurements of a water phantom are performed with different gradient fields for the three cases of (1) severe fluctuations (noisy daytime), (2) moderate fluctuations (daytime with AC), and (3) minute fluctuations (quiet midnight). It is shown that the effect of the magnetic field fluctuations on the quality of ULF-MRI measurements reduces as the applied frequency encoding gradient field increases or the active compensation is applied.

2. Theory

2.1. Effect of the field fluctuation on ULF-MRI

In an urban unshielded laboratory environment, the stability of the Earth's magnetic field is seriously impaired by environmental disturbances such as cars, subway trains, electronics devices and so on. The temporal change of the measurement field B_m, which is in total 129 μT in our experiments, reaches tens or even hundreds of nT and introduces a shift of the Larmor frequency $f_L = (\gamma/2\pi)\cdot B_m$ during multiple NMR measurements, where γ is the gyromagnetic ratio and $\gamma/2\pi = 42.57$ MHz/T for protons. This random shift spoils the averaged results and may result in both frequency and phase drift between the successive lines in k-space, leading to artifacts in the reconstructed image [14]. Note that the fluctuations in the other two environmental field components (perpendicular to B_m), which have typical drift amplitudes of tens of nT, can be ignored in the vector sum of total field strength.

In a quantitative study, the spin echo signal $s_n(t)$ of the nth phase encoding step in the two dimensional (2D) MRI experiments using standard Fourier imaging method can be written as:

$$s_n(t) = e^{-i\gamma B_m (t-T_{pe})} \iint \rho(x,z) e^{-i\gamma G_x x (t-T_{pe})} e^{-i\gamma G_{zn} z T_{pe}} dxdz \tag{1}$$

Here, $\rho(x,z)$ is the sample's proton density, G_x the frequency encoding gradient strength, G_{zn} the nth phase encoding gradient strength, x and z are the directions of frequency and phase encoding, respectively. T_{pe} is the phase encoding time, t the evolution time of imaging process. The time $t = 0$ begins at the end of the spin-flip π pulse for spin echo generation, and its duration is ignored.

In order to quantitatively determine the effect of the B_m field fluctuation on an image, we assume that the B_m field varies by ΔB_{pn} during the phase encoding time T_{pe} and varies by ΔB_{an} during the acquisition time. The signal can be re-written as:

$$\begin{aligned} s_n(t) &= e^{-i\gamma(B_m+\Delta B_{an})t + i\gamma(B_m+\Delta B_{pn})T_{pe}} \\ &\quad \times \iint \rho(x,z) e^{-i\gamma G_x x (t-T_{pe})} e^{-i\gamma G_{zn} z T_{pe}} dxdz \\ &= e^{-i\gamma(\Delta B_{an}-\Delta B_{pn})T_{pe}} e^{-i\gamma B_m (t-T_{pe})} \\ &\quad \times \iint \rho(x,z) e^{-i\gamma G_x \left(x+\frac{\Delta B_{an}}{G_x}\right)(t-T_{pe})} e^{-i\gamma G_{zn} z T_{pe}} dxdz \end{aligned} \tag{2}$$

Taking $x' = x + \Delta B_{an}/G_x$, the signal can be expressed as:

$$\begin{aligned} s_n(t) &= e^{-i\gamma(\Delta B_{an}-\Delta B_{pn})T_{pe}} e^{-i\gamma B_m (t-T_{pe})} \\ &\quad \times \iint \rho\left(x' - \frac{\Delta B_{an}}{G_x}, z\right) e^{-i\gamma G_x x' (t-T_{pe})} e^{-i\gamma G_{zn} z T_{pe}} dx'dz \end{aligned} \tag{3}$$

Comparing Eq. (3) with Eq. (1), one can notice that the B_m variation of ΔB_{pn} and ΔB_{an} will cause a position shift $\Delta B_{an}/G_x$ in the image and a phase drift $\gamma(\Delta B_{an} - \Delta B_{pn})T_{pe}$, which will result in image artifacts in both the frequency encoding direction and the phase encoding direction. The frequency shift $\Delta B_{an}/G_x$ is inversely proportional to G_x, therefore it decreases as the applied gradient field is increased, and can be ignored when it is less than the image resolution $\Delta x = \pi/[\gamma G_x(T_a - T_{pe})]$, where T_a is the acquisition time which is shortened accordingly when increasing G_x. The phase drift is proportional to the product of $(\Delta B_{an} - \Delta B_{pn})$ and T_{pe}, and can be avoided if ΔB_{pn} equals ΔB_{an}. In our environmental condition, B_m variation is dominated by the low-frequency disturbance, typically below 10 Hz. Therefore, within a single imaging step, the B_m field remains almost constant which leads to $\Delta B_{an} = \Delta B_{pn} = \Delta B_n$. In the following simulation, we will focus on discussing the frequency shift.

2.2. Numerical simulation

2D Numerical simulations were performed with $B_m = 129$ μT, corresponding to $f_L = 5.5$ kHz, and Δf_L randomly varied in the range $[-2.5, 2.5]$ Hz ($\Delta B_n \sim \pm 60$ nT). We assume a rectangular homogeneous sample with the side lengths of 40 mm and 20 mm. The MRI images were computed using the Fourier imaging method based on Eq. (2). Here, the integral ranges were $[-20, 20]$ mm and $[-10, 10]$ mm for x and z, respectively. The phase encoding time T_{pe} was taken to be 2 s, 1 s, 0.5 s, 0.35 s and 0.1 s for the applied gradient field of 12, 23.5, 47, 70.5 and 235 μT/m, respectively. 71 phase encoding steps were applied in all cases. Fig. 1(a) depicts the calculated 2D images without fluctuations (I) and with fluctuations under different gradient fields (II–IV). Fig. 1(b) shows the corresponding signal intensities vs. the coordinate axis in frequency encoding direction (horizontal axis) near the edges of images with different gradient field strengths. The figures reveal that the edges of the simulated images are strongly blurred by the field fluctuation at $G_x = 12$ μT/m. The image artifacts in the frequency encoding direction abate with increasing G_x because the frequency shift $\Delta B_n/G_x$ decreases. Furthermore, the image artifacts become invisible for $G_x = 235$ μT/m when the frequency shift is comparable to the image resolution Δx of 0.5 mm. Here, the number of averages was 50.

3. Methods

3.1. Instrumentation

The experimental results reported in this paper were obtained using a SQUID-based ULF-MRI system located in an unshielded urban laboratory environment at downtown Shanghai. The setup including the coil system, the SQUID system, a pre-polarization magnet pair, and a sample transport system, is schematically shown in Fig. 2.

The coil system consists of the measurement field (B_m) coil, 3D MRI encoding gradient coils (G_{xx}, G_{xy} and G_{xz}), the active compensation (AC) coils (B_c), and the excitation field (B_{ac}) coil. Detailed information on these coils can be found in Refs. [12,13]. The total measurement field B_m of about 129 μT was produced by the superposition of the field generated by the B_m coil and the horizontal component $B_{//}$ of the Earth's magnetic field whose vertical component ($B_\perp$) was compensated by a square Helmholtz coil (not shown in Fig. 2 for simplicity). A three-axis fluxgate (Bartington, Mag-03MSL50) was placed 3–5 m away from the center of the B_c coil to record the environmental magnetic field, and then fed back to a homemade electronics controller which drove the B_c coil to generate a reversed field and to suppress the magnetic field

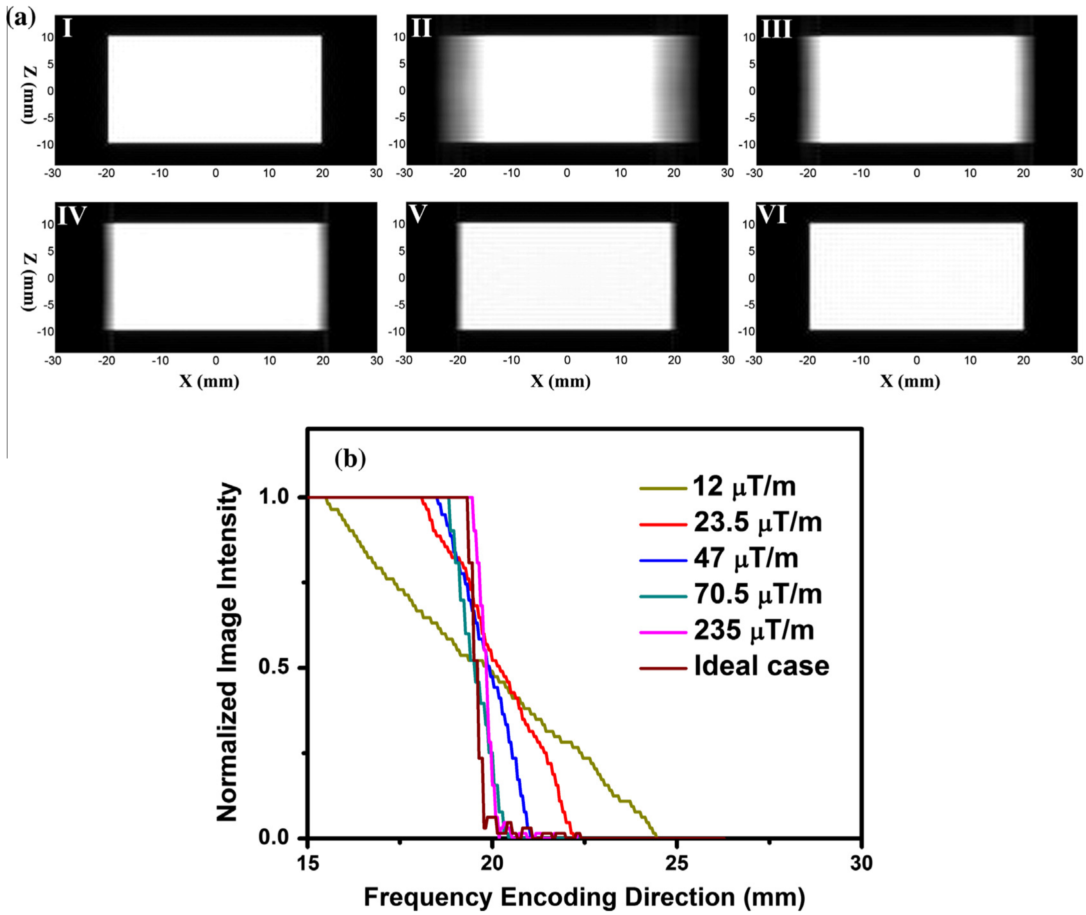

Fig. 1. (a) Simulated 2D MRI images of a rectangular homogeneous sample without fluctuations (*I*) and with fluctuations ($(\gamma/2\pi)\Delta B_n \in [-2.5, 2.5]$ Hz) while G_x and G_{zmax} = 12 μT/m (5 Hz/cm) (II), 23.5 μT/m (10 Hz/cm) (III), 47 μT/m (20 Hz/cm) (IV), 70.5 μT/m (30 Hz/cm) (V), and 235 μT/m (100 Hz/cm) (VI). (b) The signal intensities vs. the coordinate axis in frequency encoding direction near one edge of the sample for different gradient field strengths.

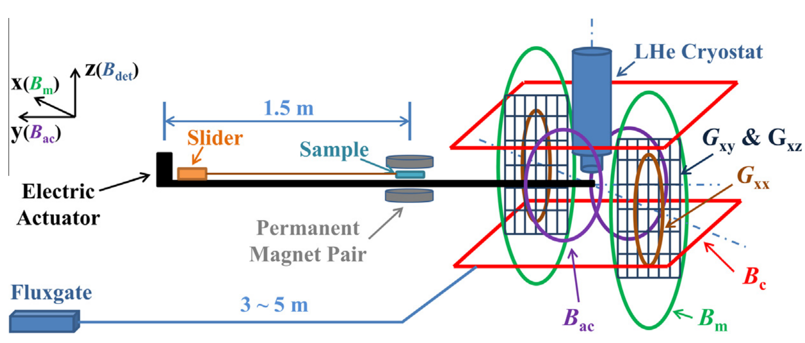

Fig. 2. Schematic of the ULF-MRI system.

fluctuation at the sample position [13]. The static environmental gradient field was balanced by using the gradient tensor compensation system. Its fluctuation can be ignored in the MRI experiments [12].

The signal was acquired by a low-T_c hand-wound second-order axial gradiometer (number of turns: 1-2-1, niobium wire diameter: 0.1 mm) which was inductively coupled to a dc-SQUID. The diameter and the baseline of the gradiometer were 22 mm and 2 × 50 mm, respectively. The gradiometer was located at the bottom of a fiberglass cryostat filled with liquid helium. The distance between the sample and the pick-up loop of the gradiometer was 15 mm. The measured spectral noise density of the SQUID system above 5 kHz was about 10 fT/$\sqrt{\text{Hz}}$.

In order to improve the signal-to-noise ratio (SNR), a 0.65 T NdFeB permanent magnet pair was used to provide a pre-polarization field. It was placed about 1.5 m away from the cryostat (the measurement position). The magnets were surrounded by a soft iron yoke, which guides the magnetic field lines and reduces their leakage, to avoid field distortion at the sample position.

A commercial electric actuator was used to automatically transport the sample between the magnets gap and the SQUID sensor.

Details on the magnet pre-polarization and on the sample transportation method in ULF-NMR/MRI measurements are given in Refs. [15,16].

3.2. Imaging parameters

The 2D imaging procedure used in our experiments is shown in Fig. 3. Each imaging step began with pre-polarization of the sample in the gap of the magnets for T_p of 5 s. Then, the sample was transported to the measurement position under the cryostat within a transportation time $T_{tran.}$ of about 1.4 s. Subsequently, a $\pi/2$ excitation field pulse was applied to tilt the sample magnetization M perpendicular to the measurement field B_m. At last, imaging was performed according to standard 2D Fourier imaging protocol with spin echo. The frequency encoding gradient G_x provided by the G_{xy} coils shown in Fig. 2 was kept on during the measurement. Spin precession was phase encoded by the gradient field G_z provided by the G_{xx} coils depicted in Fig. 2 during time T_{pe}, with G_z varying between the limiting values $\pm G_{zmax}$ with N_z phase encoding steps. The spin echo was created by applying an π excitation field pulse at the end of T_{pe}. The echo signal was measured during the acquisition time T_a with a sampling rate of 100 kHz. The most important imaging parameters are listed in Table 1.

Table 1
Imaging parameters.

G_x (μT/m)	G_{zmax} (μT/m)	N_z	T_{pe} (ms)	T_a (ms)
12	12	21	365	730
23.5	23.5	21	175	350
47	47	31	105	210
70.5	70.5	31	95	190

4. Experimental results

4.1. Fluctuations of the environmental magnetic field

The environmental magnetic field fluctuation in our laboratory was investigated using a fluxgate magnetometer. Fig. 4(a) shows the horizontal component of the environmental magnetic field in the B_m direction, measured from 8:00 PM to 8:00 AM. One can notice that during four hours in the quiet midnight (from 0:30 AM to 4:30 AM), the field fluctuation decreased to about ±1 nT from about ±100 nT in the noisy daytime. The field fluctuations in the other two directions exhibited a similar characteristic not shown here. The B_m variation causes random shifts of f_L up to several Hz, seriously spoiling the average in case of multiple measurements.

In order to suppress the magnetic field fluctuation, the active compensation system based on the spatial correlation of the low-frequency field fluctuation [13] was applied. Fig. 4(b) shows the field fluctuations in the B_m direction before and after the active compensation was used. One can see that the fluctuation was suppressed from ±100 nT to about ±10 nT, which is a moderate situation between the noisy daytime and the quiet midnight.

To observe the influence of the field fluctuation on NMR/MRI measurements, NMR experiments were performed under the three fluctuation cases: severe fluctuation (noisy daytime, $\Delta B_m \sim \pm 100$ nT), moderate fluctuation (daytime with AC, $\Delta B_m \sim \pm 10$ nT) and minute fluctuation (quiet midnight, $\Delta B_m \sim \pm 1$ nT). The 50-time averaged FID signals of a water phantom are shown in Fig. 4(c). The tap water sample was rectangular with two holes inside (see the inset in Fig. 4(c)), and its two side lengths were 30 mm and 38 mm. The B_m variation over the 50 measurements of each case caused f_L to shift 7.5 Hz, 1.5 Hz and 0.5 Hz, respectively. The averaged FID signal due to severe fluctuations in noisy daytime was seriously spoiled by the relatively large random f_L shift, e.g., its duration was greatly shortened and the signal becomes distorted. In contrast, the active compensation suppresses ΔB_n, so the FID signal was effectively recovered.

4.2. 1D and 2D MRI measurements

In order to experimentally investigate the influence of the field variation on MRI, 1D and 2D MRI measurements of the water phantom shown schematically in the inset of Fig. 4(c) were performed in the above defined three fluctuation cases when different gradient fields were applied.

Fig. 5(a) shows the spectra of 50 spin echo signals for each case with different gradient fields. One can see that the f_L variations under all the applied gradient fields were about 5 Hz, 1 Hz and 0.5 Hz for the case of severe, moderate and minute fluctuations, respectively. Fig. 5(b) shows the 50 times averaged spin echo signal of each case. No obvious differences were seen between the echo signals of moderate and minute fluctuations for all the applied gradient fields, indicating the effectiveness of active compensation. However, the averaged echo signal of severe fluctuations was smaller than those of moderate or minute fluctuations when the gradient field was weak, e.g. 12 μT/m. As the applied gradient field increased, this difference between them became smaller. Furthermore, as the gradient field was increased to about 47 μT/m, the signals of the three cases became in good accordance in our measurements.

2D MRI images of the above water phantom were obtained using the Fourier transform spin echo method. Fig. 6 shows the acquired 2D images of the sample in the three fluctuation cases with different field gradients. The results of the 2D MRI measurements exhibited a similar behavior as those of 1D MRI measurements in Fig. 5(b). The images of moderate and minute fluctuations were almost the same for all the applied gradients. The image of severe fluctuations was blurred when the gradient field was weak, e.g. 12 μT/m, and its image quality was improved

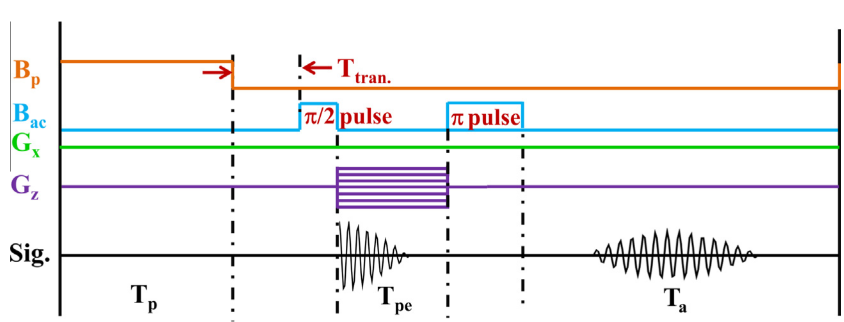

Fig. 3. 2D Fourier imaging sequence with spin echo and permanent magnets for sample pre-polarization.

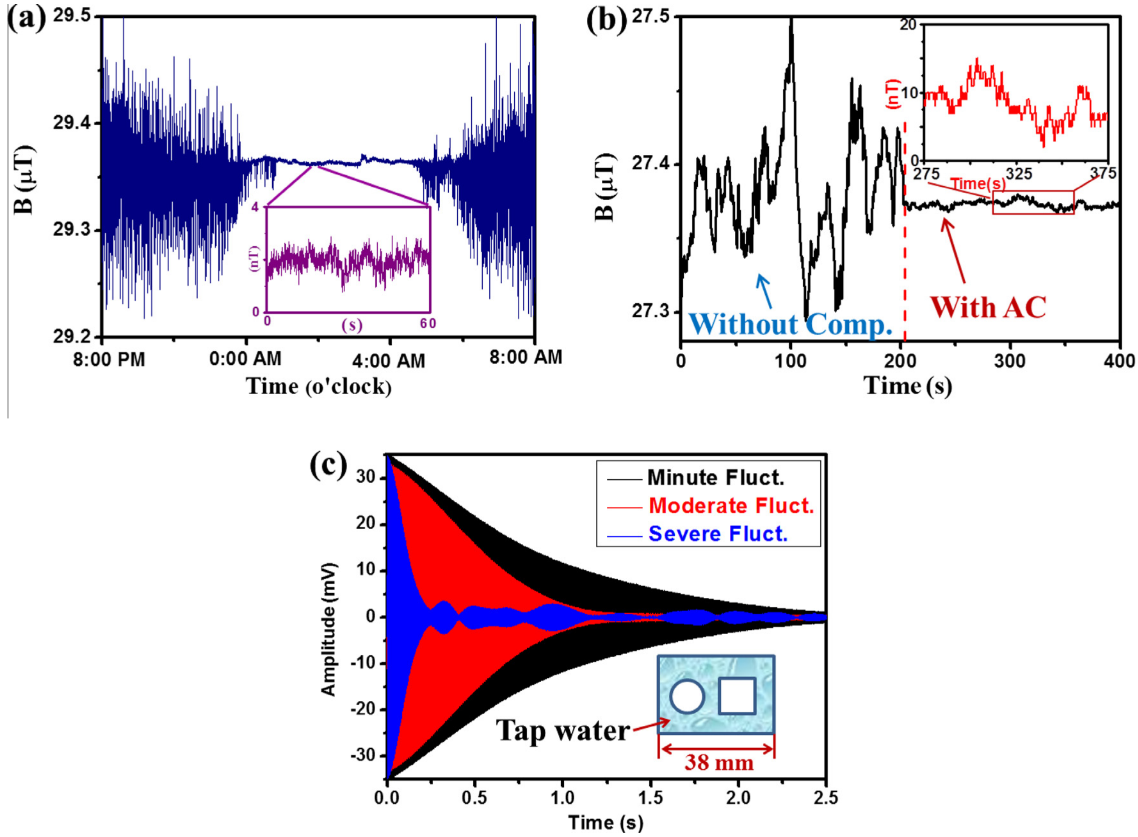

Fig. 4. (a) The horizontal component of the environmental magnetic field, recorded with a fluxgate magnetometer for 12 h. The inset shows a close-up of 60 s during midnight. (b) Magnetic field fluctuations before and after the active compensation was applied in the daytime. The inset shows enlarged fluctuation using the active compensation. (c) 50-time averaged NMR measurements of tap water in the three fluctuation cases: minute, moderate and severe fluctuation. The inset shows a schematic of the water phantom.

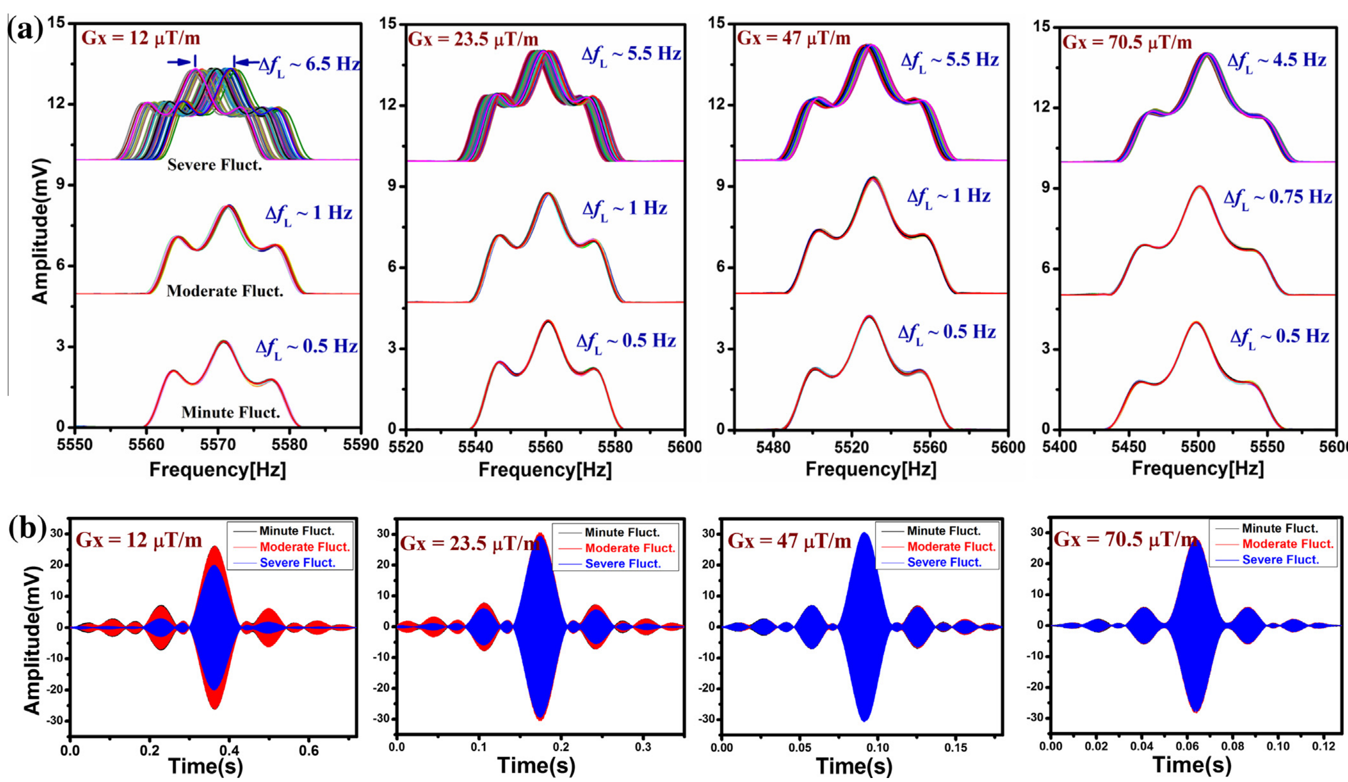

Fig. 5. (a) The spectra of 50 spin echo signals and (b) 50 times averaged echo signals of tap water in the three fluctuation cases when the applied gradient field G_x was 12 μT/m, 23.5 μT/m, 47 μT/m, and 70.5 μT/m respectively. Shifts in the longitudinal axis were made for clear display.

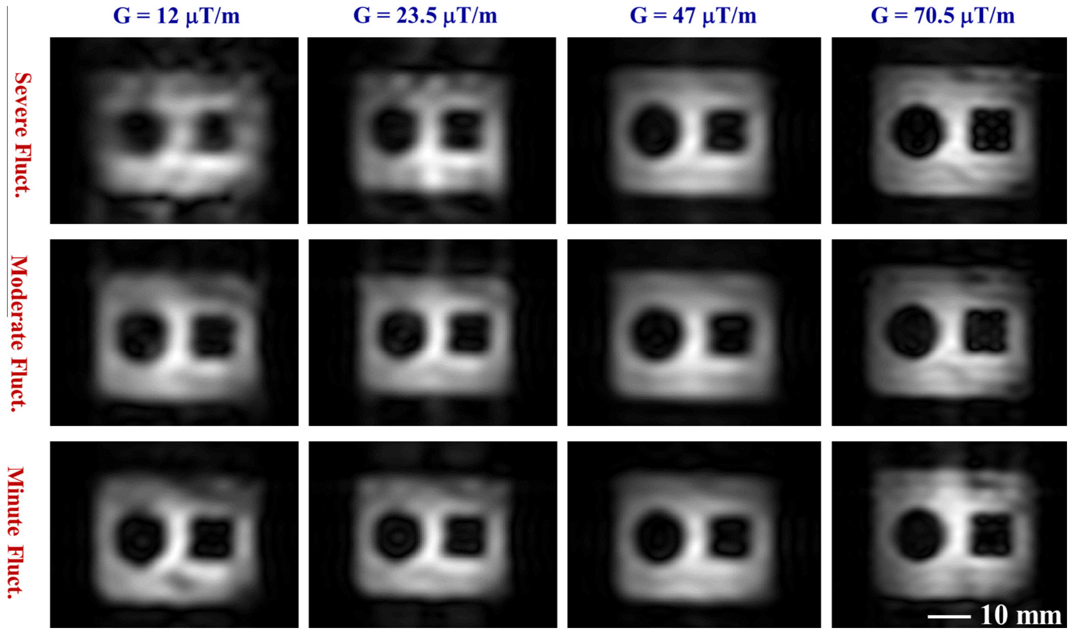

Fig. 6. 2D MRI images of the water sample depicted in the inset of Fig. 4(c) in the three fluctuation cases when the gradient field G_x and G_{zmax} was 12 μT/m, 23.5 μT/m, 47 μT/m, and 70.5 μT/m. The number of averages was 5.

as the gradient field was increased or as the active compensation was applied. When the gradient field was increased to 47 μT/m, there was no obvious difference among the three cases. These results agreed well with those of the 1D MRI measurements.

5. Discussion

The reasons for the results shown in Fig. 5(b) and Fig. 6 can be explained by comparing the frequency shift $\Delta B_n/G_x$ with the image resolution Δx. Table 2 shows the calculated frequency shifts and the image resolutions for all the applied gradients. One can notice that the frequency shifts caused by field fluctuations were less than the image resolutions in the cases of minute fluctuations and moderate fluctuations with active compensation applied, indicating that their frequency artifacts for all the applied gradients can be ignored. For the case of severe fluctuations, only when the gradient field is larger than 47 μT/m, the frequency shift became smaller than the image resolution. Then its echo signals and 2D MRI images became similar to those acquired at moderate or minute fluctuations.

In addition, as discussed above, the phase drift is proportional to the phase encoding time T_{pe}, which is usually inversely proportional to G_x, therefore the phase drift should also decrease when G_x is increased if $\Delta B_{an} - \Delta B_{pn}$ is not zero in the experiments.

The necessity of active cancelation is not obvious in our lab when the gradient field strength reaches 47 μT/m because the typical field fluctuation is only about ±100 nT. If the ambient environment becomes harsh, for example due to fluctuations of several to tens of μT induced by large magnetic objects like elevators moving up and down, the application of active cancelation may reduce the fluctuation down to the nT range. In this case, by applying sufficiently strong gradient fields in which the signal-to-noise ratio is acceptable, the artifacts in both frequency and phase encoding directions can be removed.

Table 2
Calculated shifts due to field fluctuation, and image resolution Δx for the applied gradient fields.

G_x (μT/m)	Severe fluct.	$\Delta B_n/G_x$ (mm)[a]		Δx (mm)
		Moderate fluct.	Minute fluct.	
12	13	2	1	2.7
23.5	5.5	1	0.5	2.6
47	2.7	0.5	0.25	2.3
70.5	1.5	0.25	0.17	2.1

[a] $(\gamma/2\pi)\Delta B_n$ is taken as Δf_L of the 1D MRI measurements in Fig. 5(a).

6. Conclusions

In this paper, we demonstrate the feasibility of ULF-NMR/MRI in unshielded environment under three different fluctuation conditions: severe fluctuations ($\Delta B_n \sim \pm 100$ nT), moderate fluctuations ($\Delta B_n \sim \pm 10$ nT) and minute fluctuations ($\Delta B_n \sim \pm 1$ nT). The NMR measurements were seriously affected by the field variation after averaging. However, the influence of the field fluctuations became negligible if active cancelation or the strong gradient fields were applied, so that the frequency shift $\Delta B_n/G_x$ became smaller than the spatial resolution. This result will help us to build portable and robust ULF-NMR/MRI systems working in various environments with different field fluctuation strengths.

Acknowledgments

This work was supported by the projects from Strategic Priority Research Program (B) of the Chinese Academy of Sciences (Grant No. XDB04020200), from National Natural Science Foundation of China (Grant No. 11204339), and from Natural Science Foundation of Shanghai (Grant No. 12ZR1452900).

References

[1] J. Clarke, M. Hatridge, M. Mößle, SQUID-detected magnetic resonance imaging in microtesla fields, Ann. Rev. Biomed. Eng. 9 (2007) 389–413.
[2] M. Espy, A. Matlasshov, P. Volegov, SQUID-detected ultra-low field MRI, J. Magn. Reson. 229 (2013) 1–15.
[3] M. Mößle, S.-I. Han, W. Myers, S.K. Lee, N. Kelso, M. Hatridge, A. Pine, J. Clarke, SQUID-detected microtesla MRI in the presence of metal, J. Magn. Reson. 179 (2006) 146–151.

[4] S.K. Lee, M. Mößle, W. Myers, N. Kelso, A.H. Trabesinger, A. Pines, J. Clarke, SQUID-detected MRI at 132 μT with T_1-weighted contrast established at 10 μT to 300 mT, Magn. Reson. Med. 53 (2005) 9–14.
[5] V.S. Zotev, A.N. Matlashov, P.L. Volegov, I.M. Savukov, M.A. Espy, J.C. Mosher, J.J. Gomez, R.H. Kraus Jr., Microtesla MRI of the human brain combined with MEG, J. Magn. Reson. 194 (2008) 115–120.
[6] P.T. Vesanen, J.O. Nieminen, K.C. Zevenhoven, J. Dabek, L.T. Parkkonen, A.V. Zhdanov, J. Luomahaara, J. Hassel, J. Penttilä, J. Simola, A.I. Ahonen, J.P. Mäkelä, R.J. Ilmoniemi, Hybrid ultra-low-field MRI and Magnetoencephalography system based on a commercial whole-head neuromagnetometer, Magn. Reson. Med. 69 (2013) 1795.
[7] K. Kim, S.-J. Lee, C.S. Kang, S.-M. Hwang, Y.-H. Lee, K.-K. Yu, Toward a brain functional connectivity mapping modality by simultaneous imaging of coherent brainwaves, NeuroImage 91 (2014) 63.
[8] B. Inglis, K. Buckenmaier, P. SanGiorgio, A.F. Pedersen, M.A. Nichols, J. Clarke, MRI of the human brain at 130 μT, Proc. Natl. Acad. Sci, USA 110 (2013) 19194.
[9] M. Packard, R. Varian, Free nuclear induction in the Earth's magnetic field, Phys. Rev. 93 (1954) 941.
[10] A. Mohorič, G. Planinšič, M. Kos, A. Duh, J. Stepišnik, Magnetic resonance imaging system based on earth's magnetic field, Instrum. Sci. Technol. 32 (2004) 655–667.
[11] M.A. Espy, P.E. Magnelind, A.N. Matlashov, S.G. Newman, H.J. Sandin, L.J. Schultz, R. Sedillo, A.V. Urbaitis, P.L. Volegov, Progress toward a deployable SQUID-based ultra-low field MRI system for anatomical imaging, IEEE Trans. Appl. Supercond. 25 (2015) 1601705.
[12] H. Dong, L. Qiu, W. Shi, B. Chang, Y. Qiu, L. Xu, C. Liu, Y. Zhang, H.-J. Krause, A. Offenhäusser, X. Xie, Ultra-low field magnetic resonance imaging detection with gradient tensor compensation in urban unshielded environment, Appl. Phys. Lett. 102 (2013) 102602.
[13] L. Qiu, C. Liu, H. Dong, L. Xu, Y. Zhang, H.-J. Krause, X. Xie, Magnetic field improved ULF-NMR measurement in an unshielded laboratory using a low-Tc SQUID, Phys. Proc. 36 (2012) 388–393.
[14] M.E. Halse, A. Coy, R. Dykstra, C. Eccles, M. Hunter, R. Ward, P.T. Callaghan, A practical and flexible implementation of 3D MRI in the Earth's magnetic field, J. Magn. Reson. 182 (2006) 75–83.
[15] C. Liu, Y. Zhang, L. Qiu, H. Dong, H.-J. Krause, X. Xie, A. Offenhäusser, Supercond. Sci. Technol. 25 (2012) 075013.
[16] C. Liu, Y. Zhang, H. Dong, L. Qiu, H.-J. Krause, X. Xie, A. Offenhäusser, IEEE Trans. Appl. Supercond. 23 (2013) 1601104.